Title

Photothermal Supercapacitors with Gel Polymer Electrolytes for Wide Temperature Range Operation

Journal

ACS Energy Letters, 8(4)

ISSN

2380-8195

Authors

Shin, Chanho
Yao, Lulu
Lin, Haichen
et al.

Publication Date

2023-04-14

DOI

10.1021/acsenergylett.3c00207

Peer reviewed

ACS Energy LETTERS

http://pubs.acs.org/journal/aelccp

Photothermal Supercapacitors with Gel Polymer Electrolytes for Wide Temperature Range Operation

Chanho Shin, Lulu Yao, Haichen Lin, Ping Liu, and Tse Nga Ng*

Cite This: https://doi.org/10.1021/acsenergylett.3c00207 Read Online

ACCESS | Metrics & More | Article Recommendations | Supporting Information

ABSTRACT: To deliver electrochemical energy over a wide range of temperatures, this work studies a new gel polymer electrolyte (GPE) for photothermal supercapacitors operating from −60 to 65 °C. The GPE consists of polyacrylonitrile mixed with an active filler sodium polystyrenesulfonate that simultaneously improves ionic conductivity and traps metal cation impurities. The self-discharge rate and impurity diffusion coefficients in the supercapacitors were lowered by the active filler to minimize energy loss in hot environments. For cold settings, the devices were packaged with a photothermal conversion layer that increased the internal cell temperature and raised the energy density to 94 μWh/cm^2 at the output power density of 0.4 mW/cm^2 in a −60 °C chamber. The combination of our improved GPE and photothermal conversion increased the stored energy and thereby extended the operational time of a motor driven from a cold start by a supercapacitor, demonstrating a high-performance design suitable for harsh environments.

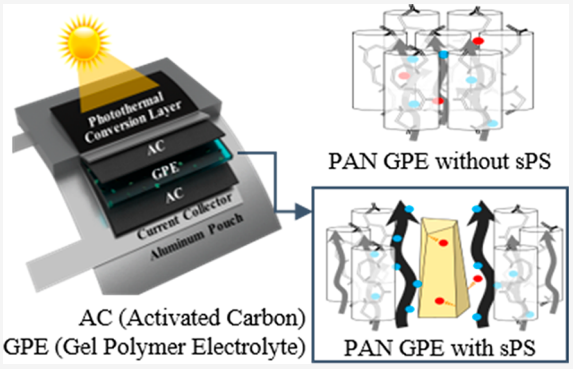

As electrochemical energy storage devices are widely used in numerous applications from portable electronics to electric transportation, the cell designs are being improved to function in different outdoor settings including cold and hot environments. At low temperature, electrochemical cells show decreased energy and power densities due to sluggish ionic transport, whereas at high temperature, device degradation is triggered by unwanted chemical reactions leading to a short cycle life and accelerated self-discharge. To tackle these issues, the engineering of electrolyte composition[1−3] can play a major role in expanding the device operational range and stability, especially in electric double layer (EDL) supercapacitors, which are more tolerant of extreme temperatures than batteries.[4,5] Thus, this work explores a novel gel polymer electrolyte (GPE), consisting of a synergistic combination of a polyacrylonitrile matrix and an ion-exchange resin filler, to advance supercapacitor performance across the temperature range from −60 to 65 °C.

Among the polymers used for GPE, polyacrylonitrile (PAN) shows excellent mechanical stability and flame resistance,[6,7] ideal for merging the electrodes' separator and the electrolyte matrix into one film. However, the ionic conductivity of PAN is limited at low temperature due to crystallization. Prior works have modified PAN with solvent plasticizers or ceramic fillers such as TiO_2, Al_2O_3, and graphene oxide to increase the amorphous phase and lower the glass transition temperature of the composite for facilitating ion transport.[8,9] Such a composite strategy is well-known, but previous studies focused on <0 °C conditions and did not consider the ramifications at elevated temperatures >25 °C. It has been observed that raising ionic conductivity often leads to an increase in self-discharge,[10,11] a phenomenon manifested by spontaneous potential decay in the open-circuit state, resulting in a loss of stored energy. To decouple this trade-off between ionic conductivity and self-discharge and in turn enable supercapacitors that work well at both low and high temperatures, we choose an active filler based on the cation-exchange resin sodium polystyrenesulfonate (sPS)[12] to mitigate a dominant self-discharge mechanism.

The combination of PAN and sPS is introduced for the GPE to simultaneously increase the ionic conductivity and suppress self-discharge in the supercapacitors. The sPS filler uniquely serves the dual functions of creating additional diffusion paths

Received: January 26, 2023
Accepted: March 21, 2023

https://doi.org/10.1021/acsenergylett.3c00207
ACS Energy Lett. XXXX, XXX, XXX−XXX

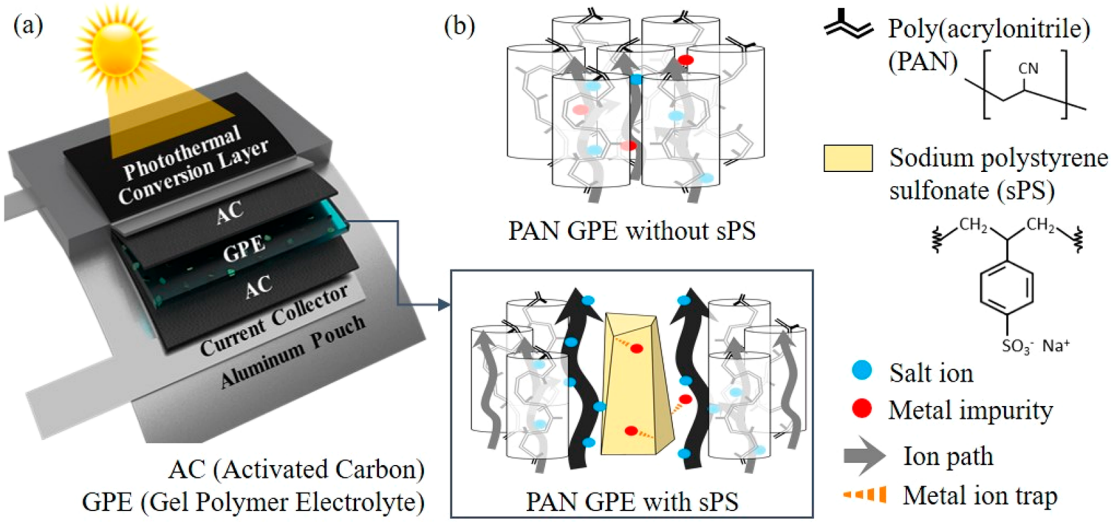

Figure 1. (a) Schematics of the photothermal supercapacitor packaged in an Al pouch. (b) Composition of the gel polymer electrolyte. The addition of ion-exchange resin sPS increases ion transport paths and scavenges metal impurities.

for electrolyte ions and scavenging transitional metal impurities, the key contributor to the diffusion-controlled self-discharge process. While the cation-exchange resin sPS is typically used in wastewater treatment to trap heavy metal cations,[13] here we leverage its preferential binding with high-oxidation-number species (≥+2) to impede the movement of impurities and thereby reduce self-discharge reactions. Meanwhile, the transport of electrolyte cations with a low oxidation number of +1 is not affected by sPS.

After characterizing the properties of the new GPE, we incorporate it into supercapacitors with activated carbon electrodes and further package the cells with a photothermal conversion layer of carbon black. The photothermal conversion layer absorbs light and converts the energy into heat due to phonon vibrations, effectively raising the cell temperature above the environmental temperature. As such, prior photothermal supercapacitors[14−19] were demonstrated to function down to −50 °C but suffer from severe self-discharge and very low energy density. In this work with the improved GPE and photothermal conversion effect, the supercapacitors are shown to operate at −60 °C, which notably is below the freezing point of the electrolyte solvent propylene carbonate (−48 °C). The following study compares the device performance and self-discharge characteristics over a wide temperature range, culminating in a demonstration of using our photothermal supercapacitor to drive a motor from a cold start and extend its run-time, toward the goal of advancing high-performance energy storage for harsh environments.

Properties of the gel polymer electrolyte (GPE). As illustrated in Figure 1a, the supercapacitor structure consisted of activated carbon electrodes separated by a GPE, enclosed in an aluminum pouch with a photothermal conversion layer on top. The GPE was comprised of polyacrylonitrile (PAN) and tetraethylammonium tetrafluoroborate ($TEABF_4$) salt dissolved in propylene carbonate (PC), either with or without sPS. The GPE compositions and preparation procedure are provided in the Experimental Methods section in the Supporting Information (Table S1). Figure 1b presents schematics on the sPS filler's roles in enhancing ion diffusion paths and trapping of metal cation impurities by the sulfonate end groups.

Figure 2a,b shows the cross-sectional morphology of GPEs without and with sPS, respectively, through scanning electron microscopy (SEM). The SEM images indicate additional free volume and increased porosity in the PAN matrix around sPS filler particles. The changes in surface morphology as a function of sPS weight percentage are presented in Supplemental Figures S1 and S2. As the outgassing of solvent during heat treatment created the porous morphology in PAN, the GPE without sPS tended to have pores perpendicular to the film surface, while the GPE with sPS showed porous structures formed around sPS because the evaporated solvent was vented to the nearby free volume.

To confirm the improvement in porosity in the GPE with sPS fillers, the specific surface area and pore size distribution were extracted from nitrogen adsorption-desorption isotherms in Figure 2c. Specific surface areas of the GPE with and without sPS were determined to be 458.7 and 268.9 m^2/g, respectively, a 1.7-fold increase in surface area from incorporating sPS. The GPE with sPS displayed a clear hysteresis loop in the relative pressure range from 0.07 to 1. The shape of the hysteresis loop, generated by differences in adsorption and desorption paths, was attributed to interactions with aggregated, nonrigid, plate-like particles.[20] The pore size distribution in Figure 2d was calculated from the isotherms according to density function theory,[20] yielding an average pore diameter of 6.8 nm in the GPE with sPS and 4.5 nm for the sample without sPS. The higher specific surface area and average pore width implied that adding sPS had led to a more porous morphology in the GPE, and these results correlated well with the SEM images in Figure 2b.

To determine the ionic conductivity in GPEs, electrochemical impedance spectroscopy was carried out to find the equivalent series resistance R of the films (Supplement Figure S3). The R_{ES} was used for calculating ionic conductivity σ with the equation $\sigma = \frac{l}{R \cdot A}$, where σ is the ionic conductivity, l is the thickness of gel polymer electrolyte, and A is the measurement area. The ionic conductivity as a function of sPS content is shown in Supplemental Figure S4. In Figure 2e, at −60 °C, the ionic conductivity of the GPE with sPS (0.99 μS/cm) was 2 orders of magnitude higher than the GPE without sPS (47 nS/

https://doi.org/10.1021/acsenergylett.3c00207
ACS Energy Lett. XXXX, XXX, XXX−XXX

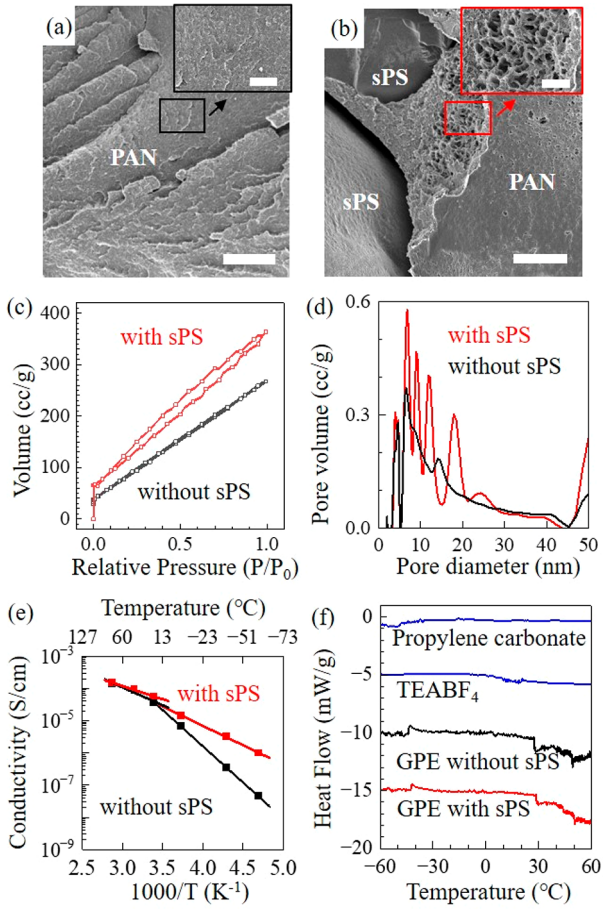

Figure 2. Cross-sectional SEM images of GPE (a) without and (b) with sPS. Scale bars: 20 μm. Insets zoom in on the polymer morphology. Scale bars: 5 μm. (c) N_2 adsorption-desorption isotherms and (d) pore size distribution curves of the GPE with and without sPS. (e) Ionic conductivity as a function of temperature measured on 100 μm thick GPE films. (f) DSC analysis of individual constituents and GPEs. Curves are offset by 5 units each in the *y*-axis for clarity.

cm). The ionic conductivity of the two GPEs converged as the temperature increased to above room temperature.

The activation energy E_A of ionic conductivity was extracted by using the Arrhenius equation $\sigma = \sigma_0 \exp\left(\frac{-E_A}{RT}\right)$, where σ_0 is the pre-exponential conductivity, R is the ideal gas constant, and T is the temperature. The fit values of E_A were 104 meV for the GPE with sPS and 194 meV for the GPE without sPS in the temperature range of −60 to 15 °C. Meanwhile, the activation energy values decreased (70—95 meV) after the transition point around 25 °C. The transition point was correlated to the glass transition temperature T_g as measured by differential scanning calorimetry (DSC) in Figure 2f. The solvent PC and salt $TEABF_4$ did not show any distinct transition in the DSC characteristics, but the GPEs exhibited a glass transition point at 30 °C. While neat PAN is known to show a T_g of ∼100 °C, the T_g of the composite GPEs was decreased by the salt and solvent serving as plasticizers.[9] From the analyses of structural and electrical properties, it is evident that sPS enhanced the electrolyte ionic conductivity by increasing the film porosity and free volume, with its effect particularly prominent at below the glass transition temperature.

Self-discharge characteristics in supercapacitors with different GPEs. The self-discharge rate was evaluated for supercapacitors fabricated using GPE with or without sPS. Self-discharge is manifested as a loss in cell potential, and it can be caused by ohmic leakage, charge redistribution, or diffusion-controlled side reactions.[12,21−25] The first two contributors can be minimized, but the diffusion-controlled side reactions are less avoidable, since carbon-based electrodes with large surface areas inevitably contain a small amount of metal impurities even under the most stringent manufacturing process. Below, we study the effect of using sPS to reduce self-discharge due to impurity reactions. In Figure 3a,b, the schematics illustrate the concept that the diffusion of metal cation impurities can be impeded because of the ion-exchange process in sPS, where the sulfonate end groups exchange their protons for metal cations with a high oxidation number. Thus, metal impurities are trapped and less likely to be transported toward the electrodes to trigger unwanted reactions leading to self-discharge. To isolate our study to diffusion effects, the measurement procedure included a holding period of 60 min at the end voltage after the charging period, as shown in Figure 3c. The holding period allowed charge redistribution to equilibrate and eliminated that mechanism from contributing to self-discharge. Subsequently, the open-circuit voltage of the supercapacitor was measured to monitor the voltage decay as seen in Figure 3d,e.

The voltage decay increased with higher temperature as side reactions were accelerated. The device without sPS showed a shift in potential decay rate after 20 min at −20 °C, but this shift might have been due to dimensional changes and contact problems with thermal contraction in the cold. Meanwhile, the sPS filler reduced the self-discharge rate across all temperatures in Figure 3f, where the m values were obtained by fitting the voltage versus time data in Figure 3d,e to the equation[10,12]

$$V(t) = V_0 - m\sqrt{t} \quad (1)$$

with

$$m = 2zFAc_i\sqrt{D}/(C\sqrt{\pi})$$

where z is the stoichiometric number of electrons in the reaction, F is Faraday's constant, A is the electrode area, c_i is the initial concentration of reacting species, D is the diffusion coefficient, and C is the device capacitance. The supercapacitor with sPS showed less self-discharge with m values lower by >17% compared to its counterpart without sPS. The self-discharge characteristics of devices using other fillers (ZrO_2 and Al_2O_3) are shown in Supplemental Figure S5, and the other fillers did not suppress self-discharge. This outcome is in agreement with our own prior results,[12] and below, we extend the previous work with additional cyclic voltammetry (CV) measurements (Figure 3g−j and Supplemental Figure S6) and analysis method to estimate a key parameter, namely, the diffusion coefficient of impurities in this system.

The diffusion coefficient can be calculated from diffusion-controlled CV data according to the Randles-Sevcik equation, which describes the current controlled by diffusion:

$$i_d = 0.4463v^{0.5}zF\left(\frac{nF}{RT}\right)^{0.5}Ac_rD^{0.5} \quad (2)$$

where v is the voltage scan rate, z is the stoichiometric number of electrons in the reaction, F is Faraday's constant, A is the electrode area, R is the ideal gas constant, c_r is the

https://doi.org/10.1021/acsenergylett.3c00207
ACS Energy Lett. XXXX, XXX, XXX−XXX

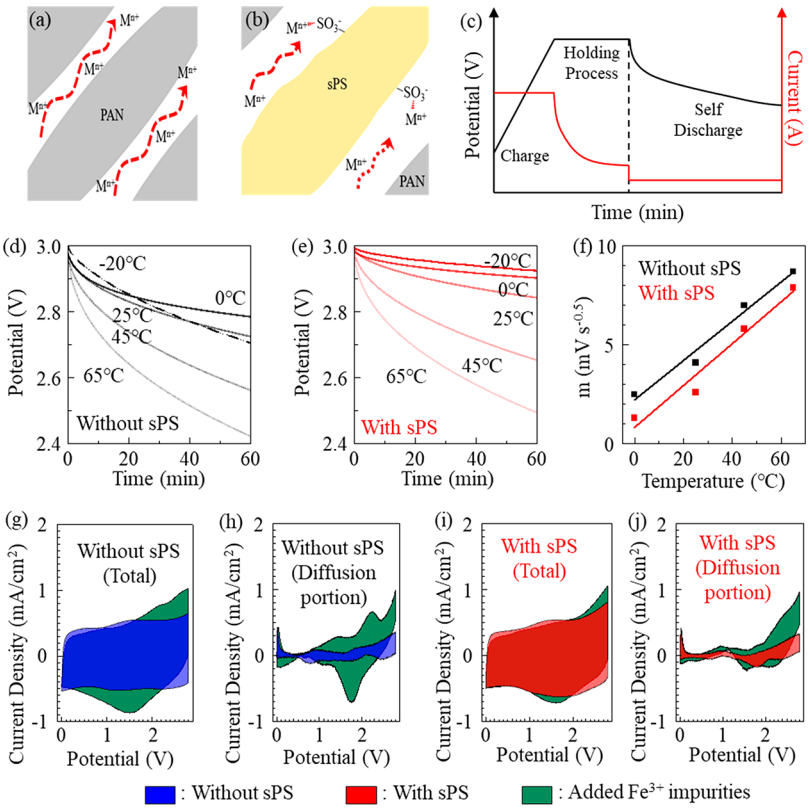

Figure 3. Schematics comparing the movement of metal impurity ions (a) in the GPE without sPS, where metal cations are freely transported across the electrolyte, and (b) in the GPE with sPS, where the sulfonate end groups capture metal cations and suppress their diffusion. (c) The potential (black line) and current (red line) profiles in self-discharge measurements. The potential is held constant for a time period to remove the contribution from charge redistribution. The start of self-discharge is indicated by the dashed line. Upon self-discharge, the voltage drop versus time was recorded at different internal temperatures for supercapacitors (d) without and (e) with sPS in the GPE. (f) The fit value of *m* in eq 1 as a function of temperature. Comparison of cyclic voltammetry for devices (g,h) without and (i,j) with sPS, measured at 45 °C and a scan rate of 1 mV/s The contribution of diffusion-limited current (h,j) was extracted from the total current (g,i) by applying eq 3. The different colors represent measurements on a device taken as fabricated (blue and red) versus a modified one, in which Fe^{3+} was intentionally added (green) to check the effect of sPS on impurity mitigation.

concentration of the reaction ions, and D is the diffusion coefficient of the reaction ions.[17,26] To determine D, the diffusion current must be extracted first from the total CV current measured at a set scan rate v, and then, the unknown parameters remaining are c_r and D. In our experiment, we intentionally added a known amount of Fe^{3+} impurities (from $FeCl_3$) to the device electrolyte; the added impurities concentration was 5.7 mM, a small amount relative to the sPS in the cell to avoid saturating it (sPS has an ion adsorption capacity[13] of 12.82 mg/g, and the added impurity concentration was 0.2 mg per 1 g of sPS, much lower than the maximum capacity). So the lower bound of c_r is known and the value of 5.7 mM is substituted into eq 2 for estimating D.

For the step of extracting the portion of CV current contributed by diffusion-controlled ion insertion process (i_d) as opposed to capacitive EDL effects (i_c), the total CV current is expressed as[27,28]

$$i(V) = i_c + i_d = k_1 v + k_2 v^{0.5} \quad (3)$$

or equivalently

$$i(V)/v^{0.5} = k_1 v^{0.5} + k_2$$

where k_1 is the capacitive-controlled constant, k_2 is the diffusion-controlled constant, and v is the scan rate. A set of CV data measured at various scan rates were obtained and plotted as $i(V)/v^{0.5}$ versus $v^{0.5}$ in Supplemental Figure S6, for which the line slope yielded k_1 and the y-intercept was k_2. With these k values, the current contribution from the diffusion-controlled mechanism was calculated and displayed in Figure 3h,j.

Comparing Figure 3h to 3g, or 3i to 3j, the diffusion-controlled current was less than 30% of the total current in as-fabricated supercapacitors (red and blue areas). Whereas after adding Fe^{3+} impurities, the diffusion-controlled current increased (green areas), although more so in the device without sPS (Figure 3h) than the one with sPS (Figure 3j). Notably, redox peaks due to Fe^{3+} were prominent at 1.7 and 2.3 V in the cell without sPS but less obvious with sPS present. The redox current at 2.3 V was 0.31 and 0.50 mA/cm^2 for the supercapacitor with and without sPS. Using these current values in eq 2, the diffusion coefficient D was calculated to be 1.48×10^{-10} m^2/s with sPS and 3.86×10^{-10} m^2/s without sPS. With this quantification, the incorporation of sPS in the GPE is shown to reduce the diffusion coefficient of impurity ions by 2.6-fold, trapping the impurities to effectively lower the self-discharge rate across the entire temperature range.

Effect of photothermal packaging on the supercapacitor performance. The supercapacitors were packaged in an aluminum pouch cell, with the surface modified with a photothermal conversion layer to take advantage of light

https://doi.org/10.1021/acsenergylett.3c00207
ACS Energy Lett. XXXX, XXX, XXX−XXX

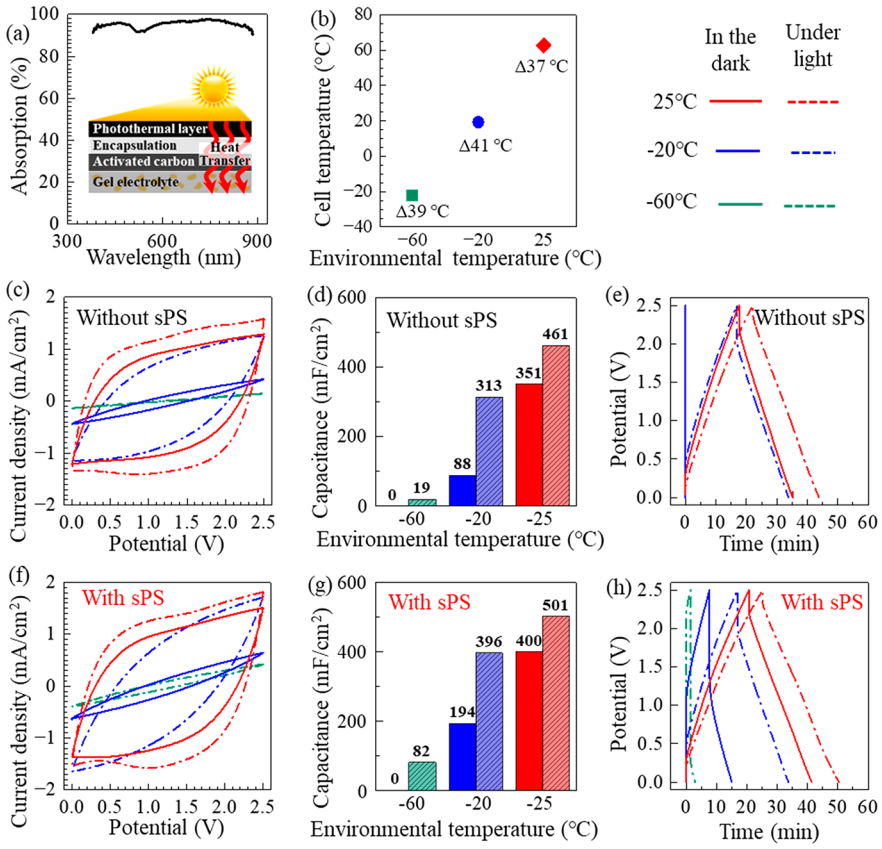

Figure 4. (a) Absorbance of the photothermal conversion layer versus wavelength. The inset illustrates photothermal conversion and heat transfer. (b) Temperature difference due to heat absorption by the photothermal conversion layer under 1 kW/m^2 of light intensity. The legends for colors and solid/dashed lines apply to all the plots in this figure. The plots in the middle row are taken on a cell without sPS and the bottom row on one with sPS. (c,f) Cyclic voltammetry curves at a scan rate of 5 mV/s. The CV data could not be measured at −60 °C in the dark. (d,g) Extracted capacitance from CV data. (e,h) Galvanostatic charge/discharge characteristics at a current density of 0.5 mA/cm^2.

Table 1. Structures and Metrics of Photothermal Supercapacitors[a]

	Electrode	GPE	Potential (V)	Illumination Intensity (kW/m^2)	Temperature (°C)	Photothermal Efficiency (%)	Energy Density (μWh/cm^2)	ref.
a	Activated Carbon	PAN/PC	2.5	1	−60/−20/25	~52.4	93.5/183/261	This work
b	CNF/Mxene@SnS_2	PVA/H_2SO_4	0.6	1	25	~86	14.7	16
c	Graphene	PVA/H_3PO_4	0.7	1	25	~18.6	0.38	17
d	LIG + Ppy	PVA/H_2SO_4	0.7	1	−30	~23.5	69.6	19
e	N-MCN@GH	PVA/H_2SO_4	1.0	3.6	−5	~32	41.3	15
f	TiN + MWCNT	PVA/LiCl	0.7	1	−40	~62.5	0.68	18
g	Activated Carbon	PVA/LiCl + glycerol	1.0	1	−50	~91.5	4.17	14
h	Activated Carbon	PVA/LiCl + glycerol	1.0	1	−20	~91.5	6.94	14

[a]CNF (cellulose nanofiber), Mxene (two-dimensional metal carbides and nitrides), LIG + Ppy (laser-induced graphene and polypyrole), N-MCN@GH (n-doped mesoporous carbon-nanosphere-intercalated 3D graphene hydrogel), MWCNT (multiwalled carbon nanotube), PVA (poly(vinyl alcohol)).

energy that could be harvested from the surroundings. The photothermal conversion layer of carbon black absorbed over 90% of the incident light as seen in Figure 4a and converted the light energy into heat due to lattice vibrations. Carbon black had a small heat capacity[29] (0.71 J g^{-1} K^{-1}) to readily pass heat to other components within the pouch. The cell temperature was monitored through a thermocouple placed inside the pouch, and the temperature differences between the environmental temperature and the cell temperature were shown in Figure 4b. With the incident light at 1 kW/m^2 (spectral characteristics of the light source provided in Supplemental Figure S7), the temperature inside the pouch was raised by 37—41 °C compared to the outside temperature. The temperature differences were similar because the conversion mechanism was the same regardless of the starting temperature. Without the photothermal conversion layer, the pouch temperature was increased by at most 6 °C compared to the environment. The photothermal conversion efficiency,

https://doi.org/10.1021/acsenergylett.3c00207
ACS Energy Lett. XXXX, XXX, XXX−XXX

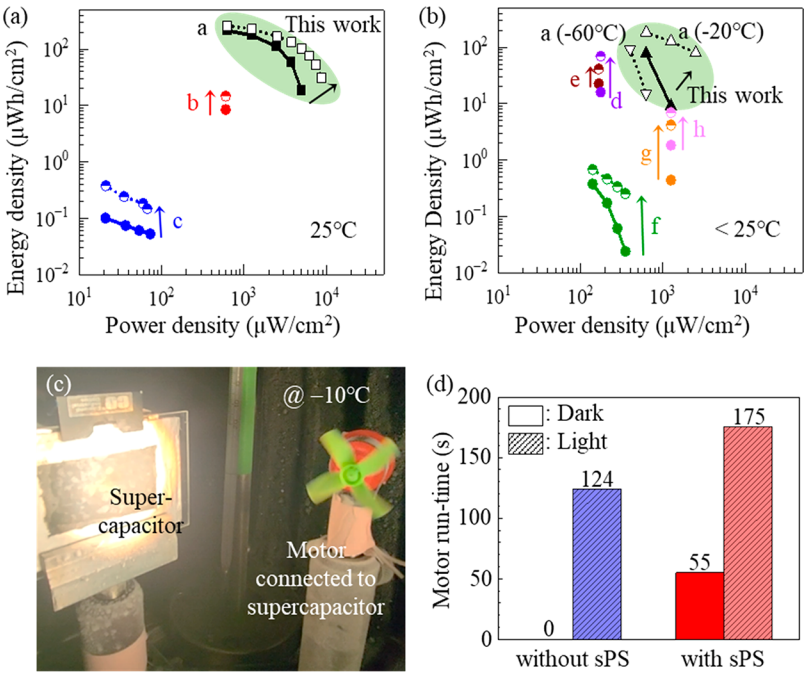

Figure 5. Comparing the performance of photothermal supercapacitors operating at (a) room temperature and (b) below room temperature. The letter labels correspond to the prior works listed in Table 1. The solid and open symbols indicate measurements done in the dark and under light with intensity shown in Table 1, respectively. At −60 °C in the dark, the devices were not working, and thus, there is no corresponding data. Meanwhile, the solid triangle symbols showed the device performance in the dark at −20 °C. (c) Photograph of a photothermal supercapacitor driving a motor at −10 °C. (d) The operating time of the motor as a function of the energy supply from supercapacitors working under different conditions.

calculated according to eq S1 with the parameter values listed in the Experimental Methods section (Table S2), was determined to be $\eta_{PT} \approx 54\%$. This efficiency was in the middle level among the photothermal supercapacitors being compared in Table 1, since our photothermal layer was made with only carbon black, unlike other references which use plasmonic materials[14,30] that increased light absorption and phonon coupling for higher heat generation. In other works, the photothermal conversion materials were incorporated in the electrodes, but this design would require the encapsulation to be transparent while there are limited choices with clear encapsulation materials. Here, we chose to separate the photothermal layer from electrodes so the devices could be fabricated with conventional aluminum pouches typically used for pouch cell encapsulation. The low specific heat of aluminum pouch encapsulation (0.89 J/K) has increased the heat transfer to the supercapacitor components and recovered the conversion efficiency.

The characteristics of photothermal supercapacitors in the dark and under 1 kW/m^2 light intensity at environmental temperatures of −60, −20, and 25 °C were compared in Figure 4c−e for the device without sPS and in Figure 4f−h for the device with sPS in its GPE. At each temperature setting, the CV curves showed current increases under illumination, because the photothermal conversion effect raised the internal temperature that increased the ionic conductivity of the GPEs and in turn improved the device capacitance. The CV data were used to find the capacitance by the equation of $C = i\Delta t/\Delta V$, where i is the current, Δt is the measurement time, and ΔV is the potential window. The extracted capacitance in Figure 4d,g showed that generally supercapacitors with sPS achieved higher capacitance due to higher ionic conductivity over all temperatures and lighting conditions.

The photothermal conversion effect was important for enabling operation at low temperature. For example at −60 °C, the devices in the dark did not work, because the electrolyte solvent PC has reached the freezing point of −48 °C. Meanwhile, under 1 kW/m^2 light, the cell capacitance was increased to 19 F/cm^2 without sPS and 82 mF/cm^2 with sPS, respectively, due to photothermal conversion effectively raising the internal cell temperature to −23 °C (Figure 4b). The photothermal effect induced more change in the device without sPS than the counterpart with sPS because of the higher activation energy for the ionic conductivity of the GPE (Figure 2e). The galvanostatic charge-discharge (GCD) characteristics in Figure 4e,h provided an additional view on the equivalent series resistance (ESR) at the start of charge/discharge step. The voltage drop due to ESR was decreased under illumination; for example, at an environmental temperature of −20 °C, the voltage drop was reduced from 1.05 V in the dark (solid blue line) to 0.45 V with a photothermal effect (dashed blue line), indicating improvement in ESR correlated to enhanced ionic conductivity.

As the supercapacitor capacitance was increased by sPS and photothermal effect, the cycling stability was maintained after 10 000 charge−discharge cycles at 25 °C, as shown in Supplemental Figure S8, where the capacitance retention was 100%. At an internal cell temperature of 65 °C, the cycling stability was >95% after 2000 cycles in the device with sPS and only 90% in the one without sPS.

Figure 5a,b compares the energy versus power densities of this work to prior photothermal supercapacitors listed in Table 1. The solid symbols are data taken in the dark, while the open symbols represent the performance under illumination. To the best of our ability, in our literature search on state-of-the-art photothermal supercapacitors, the lowest environmental

https://doi.org/10.1021/acsenergylett.3c00207
ACS Energy Lett. XXXX, XXX, XXX−XXX

temperature where the device stayed operational was −50 °C at 1 kW/m^2 illumination.[14] Here with our improved GPE with sPS, our photothermal superpcapacitor was demonstrated to work at an even lower temperature of −60 °C with the same intensity of 1 kW/m^2 illumination as previous work while achieving an areal energy density of 94 μWh/cm^2 at the output power density of 0.4 mW/cm^2 (inverted open triangle symbols in Figure 5b). At −20 °C, the photothermal conversion effect increased the device energy density to 183 μWh/cm^2 at the power output of 0.6 mW/cm^2. Here, our results exceeded prior photothermal studies and were enabled by the expanded potential window and increased ionic transport in our GPE electrolyte as well as the higher film thickness[31,32] of our activated carbon electrodes.

As a proof-of-concept demonstration in Figure 5c, our photothermal supercapacitors were used as the power source for driving a fan motor in a cold chamber of −10 °C. The charging/discharging of the supercapacitor was controlled by a single-pole-double-throw (SPDT) slide switch and a potentiostat (circuit schematics and operational voltage characteristics in Supplemental Figure S9). After the potentiostat charged the supercapacitor at a constant current of 10 mA to reach 3 V, the potentiostat was set to the open-circuit mode for measuring voltage, and the supercapacitor was connected to the motor to discharge current for powering the motor (Supplemental Video S1). This procedure was carried out in the dark and under 1 kW/m^2 illumination. Figure 5b shows the operation time of the fan motor, being dependent on the energy stored in the supercapacitor as a function of electrolyte composition and photothermal effect. The supercapacitor without sPS was not able to drive the motor in the dark but was improved by the photothermal effect to power the motor for 124 s. The supercapacitor with sPS could operate the motor both in the dark and under illumination, demonstrating a capacity to extend the motor operational time to 175 s with the assistance of photothermal conversion.

In summary, this work has demonstrated the performance of a GPE with sPS as an active filler in supercapacitors to improve capacitance and suppress self-discharge over a wide temperature range. The composite film served as a separator and solid-state electrolyte in one, leveraging the increase in porosity and ion-exchange mechanism due to sPS to enhance electrolyte ionic transport and hinder impurities from undergoing side reactions. The diffusion coefficient of impurities was lowered by nearly 3-fold through sPS, leading to better energy retention at elevated temperatures. This sPS GPE offers an economical approach to make the devices more robust against impurities inevitably present in manufacturing processes. The addition of a photothermal conversion layer on the supercapacitor pouch cell further increased the cell performance at low temperature, facilitating operation at a minimum environmental temperature of −60 °C. With the combination of sPS GPE and photothermal conversion, the supercapacitors reached state-of-the-art energy and power densities exceeding other reports on EDL photothermal supercapacitors. The supercapacitor structure in this work showed a promising design for high-performance electrochemical energy supplies in applications that span from very cold to hot environments.

■ ASSOCIATED CONTENT

Data Availability Statement

The data that support the findings of this study are available from the corresponding author upon reasonable request.

Supporting Information

The Supporting Information is available free of charge at https://pubs.acs.org/doi/10.1021/acsenergylett.3c00207.

(1) Experimental Methods. (2) Scanning electron microscopy images of electrolyte films as a function of active filler contents. (3) Electrochemical impedance spectroscopy data of gel polymer electrolyte with and without sPS measured at 0.1 Hz to 100 kHz at −60, −40, 0, 22, 45, and 75 °C under 0 V. (4) Ionic conductivity and device self-discharge characteristics as a function of filler concentration and (5) filler types. (6) CV data measured at 65 °C under voltages of 2.5 and 3. (7) Spectra of the light source, the photothermal conversion layer, and the photothermal conversion layer on an aluminum pouch. (8) Cycling stability of photothermal supercapacitors with and without sPS at 25 and 65 °C. (9) The measured potential across the supercapacitor driving a motor (PDF)

Comparison of fan motor operating time with and without sPS (MP4)

■ AUTHOR INFORMATION

Corresponding Author

Tse Nga Ng − *Material Science and Engineering Program and Department of Electrical and Computer Engineering, University of California San Diego, La Jolla, California 92093, United States*; orcid.org/0000-0001-6967-559X; Email: tnn046@ucsd.edu

Authors

Chanho Shin − *Material Science and Engineering Program, University of California San Diego, La Jolla, California 92093, United States*

Lulu Yao − *Material Science and Engineering Program, University of California San Diego, La Jolla, California 92093, United States*

Haichen Lin − *Department of Nanoengineering, University of California San Diego, La Jolla, California 92093, United States*

Ping Liu − *Department of Nanoengineering, University of California San Diego, La Jolla, California 92093, United States*; orcid.org/0000-0002-1488-1668

Complete contact information is available at: https://pubs.acs.org/10.1021/acsenergylett.3c00207

Author Contributions

C.S., L.Y., and T.N.N. designed the experiments and analyzed the data. C.S. conducted the fabrication and measurement of the devices. H.L. and P.L. contributed to the pouch cell fabrication process. The principal investigator T.N.N. conceived the gel polymer electrolyte concept and supervised the project. All authors contributed to discussions and writing of the manuscript.

Notes

The authors declare no competing financial interest.

■ ACKNOWLEDGMENTS

The authors C.S., L.Y., and T.N.N. are grateful for the support from National Science Foundation PFI-2120103 and MCA-2120701. This work was performed at the San Diego Nanotechnology Infrastructure of UCSD, which is supported by NSF ECCS-1542148.

REFERENCES

(1) Pal, B.; Yang, S.; Ramesh, S.; Thangadurai, V.; Jose, R. Electrolyte Selection for Supercapacitive Devices: A Critical Review. *Nanoscale Advances* **2019**, *1* (10), 3807−3835.

(2) Liu, S.; Zhang, R.; Mao, J.; Zhao, Y.; Cai, Q.; Guo, Z. From Room Temperature to Harsh Temperature Applications: Fundamentals and Perspectives on Electrolytes in Zinc Metal Batteries. *Sci. Adv.* **2022**, *8*, eabn5097.

(3) Zhou, L.; Cao, Z.; Wahyudi, W.; Zhang, J.; Hwang, J. Y.; Cheng, Y.; Wang, L.; Cavallo, L.; Anthopoulos, T.; Sun, Y. K.; Alshareef, H. N.; Ming, J. Electrolyte Engineering Enables High Stability and Capacity Alloying Anodes for Sodium and Potassium Ion Batteries. *ACS Energy Letters* **2020**, *5* (3), 766−776.

(4) Chaichi, A.; Venugopalan, G.; Devireddy, R.; Arges, C.; Gartia, M. R. A Solid-State and Flexible Supercapacitor That Operates across a Wide Temperature Range. *ACS Applied Energy Materials* **2020**, *3* (6), 5693−5704.

(5) Noori, A.; El-Kady, M. F.; Rahmanifar, M. S.; Kaner, R. B.; Mousavi, M. F. Towards Establishing Standard Performance Metrics for Batteries, Supercapacitors and Beyond. *Chem. Soc. Rev.* **2019**, *48*, 1272−1341.

(6) Lonchakova, O. V.; Semenikhin, O. A.; Zakharkin, M. V.; Karpushkin, E. A.; Sergeyev, V. G.; Antipov, E. V. Efficient Gel-Polymer Electrolyte for Sodium-Ion Batteries Based on Poly-(Acrylonitrile-Co-Methyl Acrylate). *Electrochim. Acta* **2020**, *334*, No. 135512.

(7) Kurc, B. Gel Electrolytes Based on Poly(Acrylonitrile)/Sulpholane with Hybrid TiO2/SiO2 Filler for Advanced Lithium Polymer Batteries. *Electrochim. Acta* **2014**, *125*, 415−420.

(8) Ma, Y.; Ma, J.; Cui, G. Small Things Make Big Deal: Powerful Binders of Lithium Batteries and Post-Lithium Batteries. *Energy Storage Materials* **2019**, *20*, 146−175.

(9) Jia, W.; Li, Z.; Wu, Z.; Wang, L.; Wu, B.; Wang, Y.; Cao, Y.; Li, J. Graphene Oxide as a Filler to Improve the Performance of PAN-LiClO4 Flexible Solid Polymer Electrolyte. *Solid State Ionics* **2018**, *315*, 7−13.

(10) Conway, B. E.; Pell, W. G.; Liu, T.-C. Diagnostic Analyses for Mechanisms of Self-Discharge of Electrochemical Capacitors and Batteries. *J. Power Sources* **1997**, *65* (1), 53−59.

(11) Haque, M.; Li, Q.; Rigato, C.; Rajaras, A.; Smith, A. D.; Lundgren, P.; Enoksson, P. Identification of Self-Discharge Mechanisms of Ionic Liquid Electrolyte Based Supercapacitor under High-Temperature Operation. *J. Power Sources* **2021**, *485*, No. 229328.

(12) Wang, K.; Yao, L.; Jahon, M.; Liu, J.; Gonzalez, M.; Liu, P.; Leung, V.; Zhang, X.; Ng, T. N. Ion-Exchange Separators Suppressing Self-Discharge in Polymeric Supercapacitors. *ACS Energy Letters* **2020**, *5*, 3276−3284.

(13) Abo-Farha, S. A.; Abdel-Aal, A. Y.; Ashour, I. A.; Garamon, S. E. Removal of Some Heavy Metal Cations by Synthetic Resin Purolite C100. *Journal of Hazardous Materials* **2009**, *169* (1), 190−194.

(14) Yu, F.; Li, J.; Jiang, Y.; Wang, L.; Yang, X.; Li, X.; Lü, W.; Sun, X. Boosting Low-Temperature Resistance of Energy Storage Devices by Photothermal Conversion Effects. *ACS Appl. Mater. Interfaces* **2022**, *14* (20), 23400−23407.

(15) Zhao, M.; Li, Y.; Lin, F.; Xu, Y.; Chen, L.; Jiang, W.; Jiang, T.; Yang, S.; Wang, Y. A Quasi-Solid-State Photothermal Supercapacitor: Via Enhanced Solar Energy Harvest. *Journal of Materials Chemistry A* **2020**, *8* (4), 1829−1836.

(16) Cai, C.; Zhou, W.; Fu, Y. Bioinspired MXene Nacre with Mechanical Robustness for Highly Flexible All-Solid-State Photo-thermo-Supercapacitor. *Chemical Engineering Journal* **2021**, *418*, No. 129275.

(17) Yi, F.; Ren, H.; Dai, K.; Wang, X.; Han, Y.; Wang, K.; Li, K.; Guan, B.; Wang, J.; Tang, M.; Shan, J.; Yang, H.; Zheng, M.; You, Z.; Wei, D.; Liu, Z. Solar Thermal-Driven Capacitance Enhancement of Supercapacitors. *Energy Environ. Sci.* **2018**, *11* (8), 2016−2024.

(18) Chen, S.; Wang, L.; Hu, X. Photothermal Supercapacitors at −40 °C Based on Bifunctional TiN Electrodes. *Chemical Engineering Journal* **2021**, *423*, No. 130162.

(19) Yu, X.; Li, N.; Zhang, S.; Liu, C.; Chen, L.; Xi, M.; Song, Y.; Ali, S.; Iqbal, O.; Han, M.; Jiang, C.; Wang, Z. Enhancing the Energy Storage Capacity of Graphene Supercapacitors: Via Solar Heating. *Journal of Materials Chemistry A* **2022**, *10* (7), 3382−3392.

(20) Bardestani, R.; Patience, G. S.; Kaliaguine, S. Experimental Methods in Chemical Engineering: Specific Surface Area and Pore Size Distribution Measurements—BET, BJH, and DFT. *Can. J. Chem. Eng.* **2019**, *97*, 2781−2791.

(21) Niu, J.; Conway, B. E.; Pell, W. G. Comparative Studies of Self-Discharge by Potential Decay and Float-Current Measurements at C Double-Layer Capacitor and Battery Electrodes. *J. Power Sources* **2004**, *135* (1), 332−343.

(22) Tevi, T.; Yaghoubi, H.; Wang, J.; Takshi, A. Application of Poly (p-Phenylene Oxide) as Blocking Layer to Reduce Self-Discharge in Supercapacitors. *J. Power Sources* **2013**, *241*, 589−596.

(23) Xia, M.; Nie, J.; Zhang, Z.; Lu, X.; Wang, Z. L. Suppressing Self-Discharge of Supercapacitors via Electrorheological Effect of Liquid Crystals. *Nano Energy* **2018**, *47*, 43−50.

(24) Wang, Z.; Xu, Z.; Huang, H.; Chu, X.; Xie, Y.; Xiong, D.; Yan, C.; Zhao, H.; Zhang, H.; Yang, W. Unraveling and Regulating Self-Discharge Behavior of Ti3C2Tx MXene-Based Supercapacitors. *ACS Nano* **2020**, *14* (4), 4916−4924.

(25) Wang, Z.; Chu, X.; Xu, Z.; Su, H.; Yan, C.; Liu, F.; Gu, B.; Huang, H.; Xiong, D.; Zhang, H.; Deng, W.; Zhang, H.; Yang, W. Extremely Low Self-Discharge Solid-State Supercapacitors: Via the Confinement Effect of Ion Transfer. *Journal of Materials Chemistry A* **2019**, *7* (14), 8633−8640.

(26) Comminges, C.; Barhdadi, R.; Laurent, M.; Troupel, M. Determination of Viscosity, Ionic Conductivity, and Diffusion Coefficients in Some Binary Systems: Ionic Liquids + Molecular Solvents. *J. Chem. Eng. Data* **2006**, *51* (2), 680−685.

(27) Augustyn, V.; Simon, P.; Dunn, B. Pseudocapacitive Oxide Materials for High-Rate Electrochemical Energy Storage. *Energy Environ. Sci.* **2014**, *7* (5), 1597−1614.

(28) Li, R.; Liu, J. Mechanistic Investigation of the Charge Storage Process of Pseudocapacitive Fe3O4 Nanorod Film. *Electrochim. Acta* **2014**, *120*, 52−56.

(29) Kelesidis, G. A.; Bruun, C. A.; Pratsinis, S. E. The Impact of Organic Carbon on Soot Light Absorption. *Carbon* **2021**, *172*, 742−749.

(30) Lin, Y.; Xu, H.; Shan, X.; Di, Y.; Zhao, A.; Hu, Y.; Gan, Z. Solar Steam Generation Based on the Photothermal Effect: From Designs to Applications, and Beyond. *Journal of Materials Chemistry A* **2019**, *7* (33), 19203−19227.

(31) Stoller, M. D.; Ruoff, R. S. Best Practice Methods for Determining an Electrode Material's Performance for Ultracapacitors. *Energy Environ. Sci.* **2010**, *3* (9), 1294−1301.

(32) Yao, L.; Liu, J.; Eedugurala, N.; Mahalingavelar, P.; Adams, D. J.; Wang, K.; Mayer, K. S.; Azoulay, J. D.; Ng, T. N. Ultrafast High-Energy Micro-Supercapacitors Based on Open-Shell Polymer-Graphene Composites. *Cell Reports Physical Science* **2022**, *3*, No. 100792.

https://doi.org/10.1021/acsenergylett.3c00207
ACS Energy Lett. XXXX, XXX, XXX−XXX